Eur. Phys. J. B **5**, 283–297 (1998)

THE EUROPEAN PHYSICAL JOURNAL B

Spatio-temporal patterns in the thermoconvection of a planar nematic layer: II. Experiments

E. Plaut[a,b], L. Pastur, and R. Ribotta

Laboratoire de Physique des Solides, Université Paris-Sud, 91405 Orsay Cedex, France

Received: 1st December 1997 / Revised: 25 May 1998 / Accepted: 2 June 1998

Abstract. We study experimentally the evolution of thermoconvection in a laterally extended planar nematic layer, at zero or weak stabilizing magnetic field. As the applied thermal gradient is increased, a cascade of symmetry breakings occurs, towards structures of increasing spatial complexity, and ultimately towards oscillating states. The patterns are characterized optically, and simple models for the distortion of the vertical (out of plane) component of the director field are proposed.

PACS. 47.54.+r Pattern selection; pattern formation – 47.20.Bp Buoyancy-driven instability – 42.70.Df Surface-tension-driven instability

1 Introduction

We present here experimental results on the thermoconvection of a planar nematic layer, and we compare them with the theoretical models of the first part [1] and of [2]. Thermoconvection of a planar nematic layer is a model system for pattern formation in anisotropic geometry. It is obtained by heating from below a horizontal layer of nematic liquid crystal with planar anchoring boundary conditions: the director $\mathbf{n}$ is set in a horizontal direction $\hat{\mathbf{x}}$ at the plates. Previous experimental studies have been done in [3,4], but only rather small aspect ratios were achieved ($\Gamma = \text{width/thickness} \lesssim 15$). This renders the comparison with the existing nonlinear theories [1,2] questionable. In effect, these theories consider the layer to be infinitely extended in the horizontal plane, in order to use Fourier-space techniques. Also, in the most recent experiments [4] a fairly large stabilizing magnetic field $\mathbf{H} = H\hat{\mathbf{x}}$ was applied, which progressively "freezes" the director field in the $\hat{\mathbf{x}}$ direction. Thus, since the first studies of the linear properties of the system [3] no systematic experiments have been performed in the intrinsic regime of the null or small magnetic fields H. In this regime, the director is by far the weakest damped field, and should therefore control the dynamics of the system: this is a "director-dominated regime" (DDR) [5]. In this paper we investigate precisely the nonlinear evolution of planar thermoconvection in the DDR.

In Section 2 the experimental setup and methods are described. The properties of the system near threshold are discussed in Section 3. Sections 4 and 5 are concerned with the evolution of the system in the nonlinear regime, when the reduced control parameter $\epsilon = \Delta T/\Delta T_c - 1$ (ΔT_c = threshold value of the applied temperature difference ΔT) is adiabatically increased. We describe in Section 4 the cascade of (quasi) stationary structures found in a first ϵ range. In particular, a detailed study of the main convective amplitude is performed (Sect. 4.2), which shows clearly the limits of the weakly nonlinear models. We present in Section 5 the subsequent structures, which are oscillating. The whole cascade is shown in Figure 15, which summarizes our main results.

The spatio-temporal structures have been characterized by optical studies of the director field [6]. We give simple models for the distortion of the vertical component n_z of the director, assuming to leading order:

$$n_z(\mathbf{r}, z) = n_z(\mathbf{r}) \cos(z) \tag{1.1}$$

where $\mathbf{r} = x\hat{\mathbf{x}} + y\hat{\mathbf{y}}$ is the horizontal position, and the lengths are scaled as in [1] in units of d/π, where d is the layer thickness (then the layer extends between $z = -\pi/2$ and $\pi/2$). The models given for $n_z(\mathbf{r})$ also contain only the leading order, and introduce amplitudes in the spirit of the envelope approach [7]. These models will allow for a good reconstitution of the experimental patterns.

2 Experimental setup and methods

2.1 Experimental setup

An important difference between classical thermoconvection (*i.e.* thermoconvection in isotropic fluids, or thermoconvection in a planar nematic at very large planar magnetic field) and DDR nematic thermoconvection is the fact

[a] e-mail: `plaut@theo-phy.uni-bayreuth.de`

[b] *Present address:* Physikalisches Institut der Universität Bayreuth, 95440 Bayreuth, Germany.

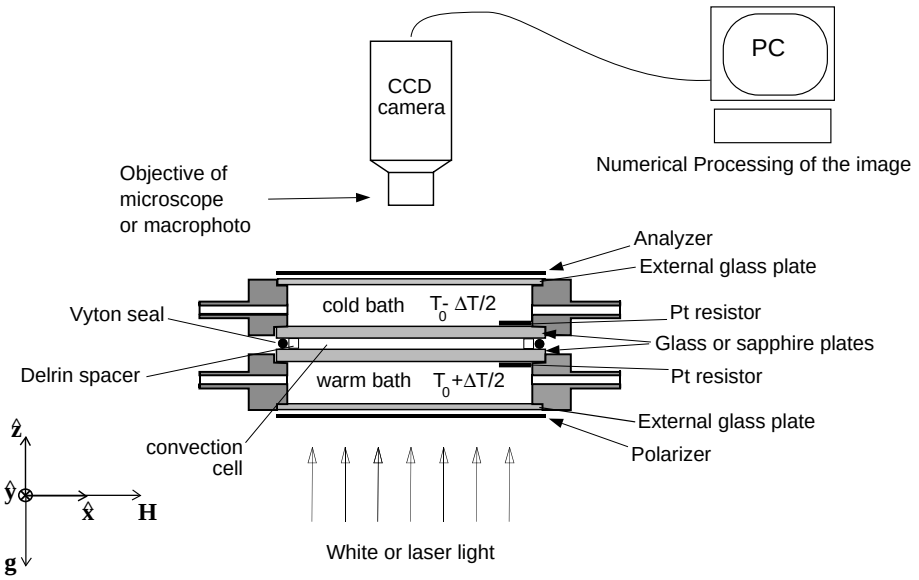

Fig. 1. Schematic diagram of the experimental setup, which consists of two thermal bath enclosing a horizontal convection cell (**g** is the earth gravity field). Typically, the width of the cell is $\simeq 10$ cm, and its thickness is $d \simeq 1.3$ mm. The cell is filled with nematic liquid crystal aligned in the direction $\hat{\mathbf{x}}$ at the plates. These plates are either sapphire or glass (see text). The whole arrangement permits observation in transmitted light. It is placed in the air-gap of a large electromagnet (not shown), which applies a planar magnetic field **H** parallel to $\hat{\mathbf{x}}$.

that the temperature and velocity modulations are in the latter case quite small (see Eq. (4.13) of [1]). Consequently, the standard heat-flux measurements techniques should be rather inadequate in this system. Moreover, mixing a large number of small particles in the nematic without strongly perturbing the convective structures is almost impossible because of the small thickness of the cells. Thus the standard velocimetry techniques should also be barely applicable there. For these reasons, and because the director field **n** is expected to play the most important role in the instabilities, one would rather prefer to have access to **n**. This is possible with optical methods, which are easier to develop in transmitted light than in reflected light as in the standard setup for thermoconvection. We therefore chose to realize a symmetric and totally transparent setup. The use of transmitted light also diminished the loss of intensity due to the scattering in the nematic. The nematic layer is sandwiched between two glass or sapphire plates in contact with thermal baths, themselves enclosed by glass plates (Fig. 1). This allowed us to develop new optical methods [6] using linearly polarized light: either the "extraordinary light" polarized along $\hat{\mathbf{x}}$, or the "ordinary light" polarized along $\hat{\mathbf{y}}$. The images shown hereafter were taken from above with a CCD camera equiped with a macrophoto objective, and digitized on a grid of 512×512 pixels in 256 gray levels on a Personal Computer. Their numerical Fourier transform was also used to characterize accurately the patterns.

Each thermal bath was permanently fed by flowing water coming from two Lauda RC 6 temperature regulators, which presented a stability of $\pm$ 0.015 °C. The applied thermal difference ΔT was measured against the external sides of the plates enclosing the convection cell by two Pt resistors. This showed that the same stability of $\pm$ 0.015 °C was reached for ΔT. A limitation of the RC 6 temperature regulators is that the smallest change of temperature that they can achieve is of the order of 0.05 °C. This value defined our experimental resolution in ϵ (Fig. 4b):

$$\delta\epsilon = \frac{0.05\,^{\circ}\mathrm{C}}{\Delta T_c}\cdot \tag{2.1}$$

Three different cells were realized: cell 1 was square (of 100 mm side) and with glass plates (BK10 from Schott); cells 2 and 3 were cylindrical (of radius 90 mm) and with sapphire plates (from Rubis SA). A Vyton seal ensured the tightness, and the thickness d of the cells was controlled by a Delrin spacer. Locking screws tightening the upper and lower part of the cell were used to press the two internal transparent plates onto the spacer and the seal, such that the seal was completely flatten out. For cell 1, $d = 1.00 \pm 0.04$ mm, for cell 2, $d = 1.30 \pm 0.01$ mm and for cell 3, $d = 1.520 \pm 0.001$ mm, as tested by interferometry. Thus we reached the largest aspect ratios obtained so far in nematic thermoconvection, *i.e.* taking into account the width of the seal and spacer:

$$\Gamma = \frac{\text{width of the fluid layer}}{d} = \begin{array}{l} 87.5 \text{ for cell 1,} \\ 63 \text{ for cell 2,} \\ 53 \text{ for cell 3.} \end{array}$$

The corresponding small parameter is the smallest wavevector δq attainable in the experiments, *i.e.* with

lengths in units of d/π:

$$\delta q = \frac{d}{\pi}\,\frac{2\pi}{\lambda_{max}} = \frac{d}{\pi}\,\frac{2\pi}{\Gamma d} = \frac{2}{\Gamma} = \begin{array}{l} 0.023 \text{ for cell 1,} \\ 0.032 \text{ for cell 2,} \\ 0.038 \text{ for cell 3.} \end{array} \quad (2.2)$$

The quality of the thermal boundary conditions at the plates (ideally $T = const.$) is defined by the ratio (ideally ∞):

$$r = \frac{\text{heat conductivity of the plates}}{\text{heat conductivity of the nematic}} \simeq \begin{array}{l} 9 \text{ for cell 1,} \\ 270 \text{ for cells 2 and 3.} \end{array}$$

There, we have used as a typical value for the heat conductivity of the nematics 0.15 $\mathrm{Wm^{-1}K^{-1}}$ (see the references in Appendix A of [1]), whereas the values of the heat conductivities of the plates were obtained from the makers. A first important result of our experiments is that the sequence of transitions in the nonlinear regime was the same in all cells. It shows firstly that the shape of the cell has a little influence on the convection structures, as it is expected in the large aspect-ratio limit. Secondly, it proves that the thermal boundary conditions play a minor role in our case, *i.e.* that the fine details of the temperature field have no influence on the dynamics: this confirms that the dynamics is dominated by the director field.

The planar anchoring was realized by coating the internal surface of the plates with a polymer (ZLI 2650 from Merck), curing, and rubbing using a specific device. The unidirectionality was rather good, as can be inferred from the zig-zag structures at $H = 0$ shown in Figure 2: the axis of symmetry of the zig-zags, which is given by the anchoring direction, is well defined. The whole cells were made of non-magnetic materials, and placed in the air-gap of a large electromagnet. Its polar heads have been reshaped so as to ensure a good uniformity of the magnetic field over the space of the cell, where it varied of less than $\pm$ 0.7%.

We used the nematic materials (Appendix A of [1]) MBBA, which was synthesized in our laboratory; and 5CB, which we obtained from Merck. We used successively both nematics in every cells, at a working temperature of 27 °C (*i.e.* well inside the nematic phase). We always observed the same sequence of transitions in the nonlinear regime. Most of our quantitative measurements have been performed in cell 3 with 5CB, which showed a better chemical stability than MBBA. Typical values of the characteristic Fréederickz field are the one calculated for cell 3:

$$B_{\mathrm{F}} = \mu_0 H_{\mathrm{F}} = \frac{\pi}{d}\sqrt{\frac{k_{11}}{\frac{\chi_a}{\mu_0}}} = \begin{array}{l} 47.3 \text{ G for MBBA,} \\ 46.5 \text{ G for 5CB.} \end{array}$$

In the following, we will use for the planar magnetic field $\mathbf{H} = H\hat{\mathbf{x}}$ the reduced variable $h := H/H_{\mathrm{F}}$.

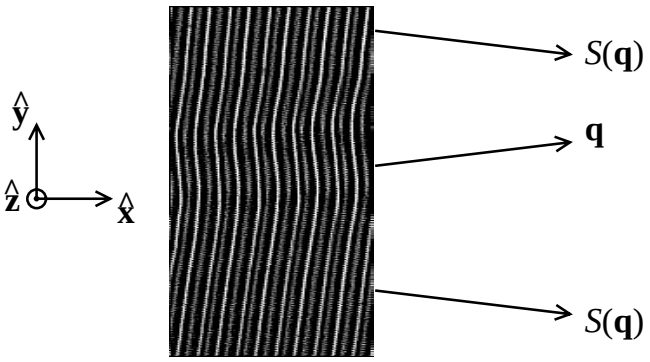

Fig. 2. Zig-zag structure in 5CB in cell 3, at $H = 0, \epsilon = 0.06$. The structure is observed from above in extraordinary light: the bright "caustic" lines indicate the centers and edges of the rolls (an edge-detection filter has been used to enhance the contrast). Three roll domains are visible, where the wavevector of the rolls is either $\mathbf{q}$ or its symmetric $S(\mathbf{q})$ under S: $\hat{\mathbf{y}} \mapsto -\hat{\mathbf{y}}$. The direction of symmetry $\hat{\mathbf{x}}$ is defined only by the planar anchoring, since there is no magnetic field applied.

2.2 Experimental procedure for the control parameter ramps

Our experiments were typically done by slowly increasing the control parameter ϵ ("ϵ-ramp"). To prepare such a ramp, we keep the system during one hour at null thermal gradient $\Delta T = 0$ (*i.e.* $\epsilon = -1$) and under a strong planar magnetic field $h \simeq 20$. Thus all director relaxation times are reduced to a few seconds, whereas the horizontal relaxation times of the temperature and velocity fields (which are much longer, up to ≈ 2000 s in cell 2) are also largely overstepped. This ensures that the previous director, temperature and velocity modulations relax totally.

The main experimental difficulty stems from the very long characteristic times τ of the system (see Sect. 3 and Fig. 4a). One has to choose a compromise for the velocity of the ϵ-ramps made by increasing ϵ by steps equal to the experimental resolution $\delta\epsilon$ (2.1). These ramps must be performed in a reasonable interval of time (less than a few weeks), during which the overall stability of the system can be insured. On the other hand, these ramps must be slow enough to insure that the first threshold and the thresholds of the transitions in the nonlinear regime are measured with an accuracy of the order of $\delta\epsilon$. One must be sure that no instabilities are overlooked between two ϵ steps. If the threshold ϵ_0 of a transition has just been passed, the amplitude of the corresponding perturbation, which starts from a very small "noise" value, must reach a value large enough such that the perturbation becomes visible before the next ϵ step. Since the growth rate of the perturbation is typically in $a\tau^{-1}\ (\epsilon - \epsilon_0) \simeq a\tau^{-1}\delta\epsilon$, an amplification by a factor e^2 will be realized in an interval δt given by $\delta t \simeq 2\tau/(a\ \delta\epsilon)$. Assuming a of order 1, we chose as a minimum waiting time between two ϵ steps:

$$\delta t = 2\frac{\tau}{\delta\epsilon}\cdot \quad (2.3)$$

With this choice, we already have $\delta t(h = 0) = 9$ hours (Fig. 4b), which is a rather long time. Our ϵ-ramps were then started as follows:

- for the first ramp at a given h, since $\Delta T_c(h)$ is not yet measured, we start the ramp at $\Delta T \simeq 0.85\ \Delta T_c$ using the theoretical value for ΔT_c. We then increase ΔT by steps of 0.05 °C, waiting a time δt after each step. If no director modulation in extraordinary light (where the optical sensitivity is higher) is observed after this interval, we further increase ΔT. This gives us the threshold with a precision of 0.05 °C;
- when $\Delta T_c(h)$ is known, we start directly the ramp at $\epsilon \simeq 0$, and increase ϵ of $\delta\epsilon$ after the interval δt if the convection does not develop.

We are then "at threshold", *i.e.* at $0 < \epsilon < \delta\epsilon$. When a stationary structure is reached (within an interval of a few δt, see Sect. 3), the ramp is carried on exactly the same way:

- after increasing ϵ by $\delta\epsilon$, we wait for a time δt;
- if no structural change has occurred (not taking into account the increase of the convective amplitude), we increase ϵ further;
- otherwise we wait until a new stationary structure, or a permanent regime (we test it on an interval of a few δt), is reached.

With some slower ϵ-ramps, we checked that the transition thresholds are the same (with an accuracy $\pm\ \delta\epsilon$), whereas with faster ramps some thresholds were shifted (of more than $2\delta\epsilon$): thus this procedure seemed rather optimal. Nevertheless, we did not test with slower ramps for all h and for all transitions.

3 The normal rolls and the dynamics of their undulations at threshold

Firstly, we compared in our sapphire cells the experimental threshold values ΔT_c with the theoretical values

$$\Delta T_c = \frac{\nu_a \kappa_\perp \pi^4}{\alpha g d^3} R_c$$

where R_c is a dimensionless threshold [1]. A good agreement with a mean error $< 4\%$ (see *e.g.* the first line in Fig. 15) is obtained provided that the thermal expansion coefficients α are taken to be $\alpha_{\mathrm{MBBA}} = 1.1 \times 10^{-3}\ \mathrm{K}^{-1}$, $\alpha_{5\mathrm{CB}} = 1.0 \times 10^{-3}\ \mathrm{K}^{-1}$. The value for MBBA is consistent with the former estimation $\alpha_{\mathrm{MBBA}} \simeq 10^{-3} - 10^{-4}\ \mathrm{K}^{-1}$ [3,8]. The value for 5CB matches the measurement $\alpha_{5\mathrm{CB}} = 9.1\ 10^{-4}\ \mathrm{K}^{-1} \pm\ 10\%$ made in [9].

We observe at threshold roll patterns (Fig. 5) with a mean wavevector (barycenter of the main Fourier spot) $\mathbf{q}_0 = q_c \hat{\mathbf{x}}$ of the *normal roll* (NR) type: the rolls have globally their axis normal to the anchoring direction $\hat{\mathbf{x}}$, as predicted by the linear theory. Observations in ordinary light, where the contrast is proportional to $n_z^2(\mathbf{r})$ [6], show

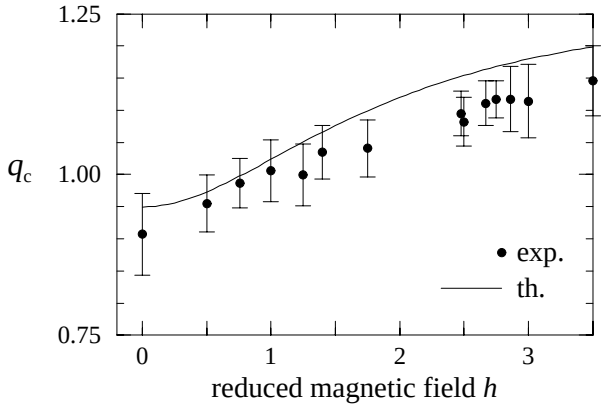

Fig. 3. The normal roll wavevector q_c for 5CB in cell 3. The experimental points are compared with the values predicted by the linear theory (solid line). q_c has been scaled in units of π/d where d is the layer thickness (see Table 1 of [1]).

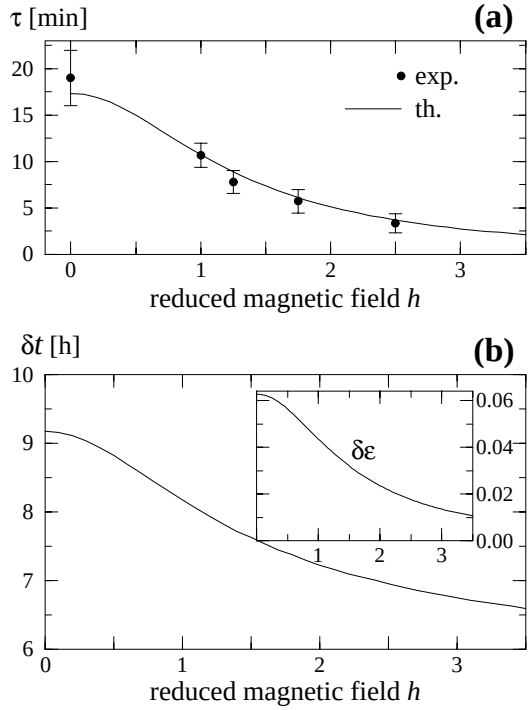

Fig. 4. (a) The characteristic time τ of the instability for 5CB in cell 3, compared with the predictions of the linear theory (solid line). (b) The minimum time δt between two ϵ steps during the control parameter ramps, as deduced from the linear theory with equation (2.3). Inset: ϵ resolution from equation (2.1).

that NR can be described in a first approximation by a local director field:

$$n_z(\mathbf{r}) = A\ \sin \mathbf{q}_0 \cdot \mathbf{r}. \tag{3.1}$$

Our measured values of q_c agree (within $\pm\ 4\%$) with the predictions of the linear theory for the critical wavevector (Fig. 3). We also studied the exponential

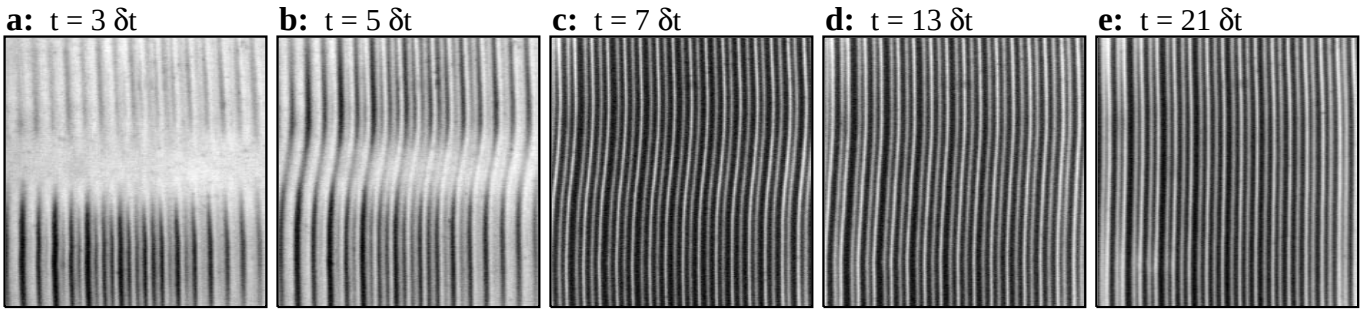

Fig. 5. Evolution of convection patterns after a step from below to above threshold ($\epsilon \simeq 0.01$) at $t = 0$, with 5CB in cell 3 at $h = 1.5$. For this value of the reduced magnetic field, one has $\delta t = 7.5$ h, and the last image was taken one week after applying the step. The patterns are observed in extraordinary light.

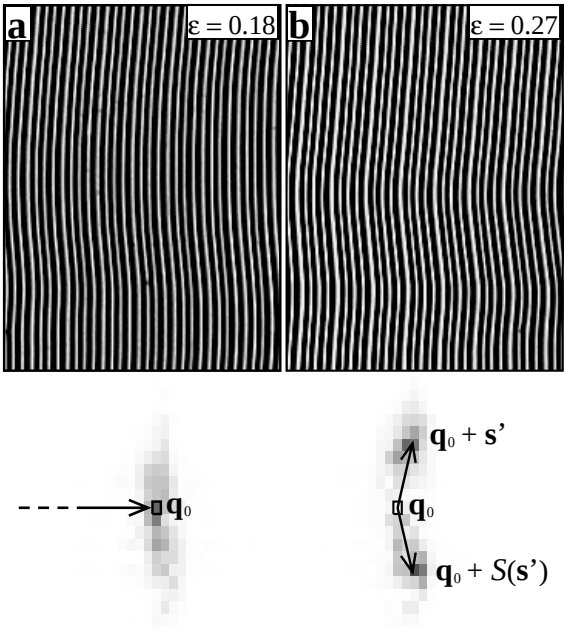

Fig. 6. Transition (a) undulated rolls → (b) zig-zag structures, with 5CB in cell 3 at $h = 1.75$, observed in extraordinary light. Below each image is represented its main Fourier spot numerically computed. The surrounded pixel $\mathbf{q}_0$ is the mean wavevector of the initial structure, *i.e.* the barycenter of the (a)-Fourier spot. A pixel height is of the order of δq defined in (2.2).

relaxation of the rolls after a step now to below the threshold, with the optical technique developed in [6] to measure A in (3.1).

The deduced characteristic times (Fig. 4a) agree rather well with the predictions of the linear theory. Thus it is justified to use these predictions in order to define $\delta\epsilon$ and $\delta t(h)$, as was done in Section 2.

In fact, whereas *at high magnetic field* $h \gtrsim 1.75$ a NR pattern is always obtained as soon as the amplitude has saturated, the situation is more intricate for smaller fields. A representative example of the development of convection at *not too small magnetic fields* $h \gtrsim 1$, after a step from below to just above threshold ($0 < \epsilon < \delta\epsilon$), is shown in Figure 5. Though the NR consistent with theory are finally obtained (Fig. 5e), one observes a very long relaxation process *via undulated rolls* (UR). The generation of UR can be understood from an inspection of Figures 5a, b, c. In Figure 5a, NR nucleate spontaneously at different places with uncorrelated phases, since specific lateral boundary conditions are not used to set the roll phase (indeed the lateral walls, in all the cells of various shapes, appeared to have no influence on the convection rolls at threshold). The roll domains of Figure 5a then connect through an undulation in Figures 5b and c; obviously the UR have been induced by the natural inhomogeneities in the development of convection. These UR can be modeled, in a idealized homogeneous case, by the superposition

$$n_z(\mathbf{r}) = A\ \sin \mathbf{q}_0 \cdot \mathbf{r} + a(t)\ [\sin(\mathbf{q}_0 + \mathbf{s}) \cdot \mathbf{r}\ -\ \sin(\mathbf{q}_0 - \mathbf{s}) \cdot \mathbf{r}] \quad (3.2)$$

with $a(t) \ll A$, $\mathbf{s} = p\hat{\mathbf{y}}$. This superposition leads to a $n_z(\mathbf{r})$ profile in $A\sin(q_c x) + 2a(t)\cos(q_c x)\sin(py)$ typical of UR. This simplified model can also be justified by the fact that the main Fourier spot of UR presents a large extension along $\hat{\mathbf{y}}$, and is roughly symmetric under the application of $S : y \mapsto -y$ (Fig. 6a). In practice the wavevector $\mathbf{s}$ in (3.2) is only defined as the barycenter of the half-Fourier spot in the region $y > 0$; this wavevector $\mathbf{s}$ appears to be selected (in a complicated manner) by the overall geometry and the extension of the original phase domains. The hypothesis $A = const.$ in (3.2) is confirmed by the fact that the optical contrast of the rolls does not change from Figures 5c to 5e, *i.e.* that the saturation of the amplitude has occurred. The secondary amplitude $a(t)$ can then be extracted from a Fourier transform of the patterns. It shows typically an exponential decay: the UR are *transient*. In the case of Figure 5, we measure in this way for the UR relaxation time $\tau_{UR} \simeq 9\ \delta t$. Theoretically, the UR (3.2) correspond exactly to the pattern (Eqs. (5.1, 5.4) of [1]) expected at the onset of a long-wavelength zig-zag instability, and for which a relaxation time (see Eq. (5.5) of [1] and Eq. (3.3) below) has been calculated in the framework of the lowest-order amplitude equation. At $h = 1.5$, from the theoretical values $\delta\epsilon = 0.03$, $\xi_{yy} = 0.45$, and with $p = 0.1$ as an estimate of the wavevector of the UR of Figures 5b, c (value deduced from the Fourier transform), we get $\tau_{UR} = \tau(h)/(\xi_{yy}^2(h)\ p^2) \simeq 8\ \delta t$. There is an agreement between the experimental and theoretical UR relaxation time, and

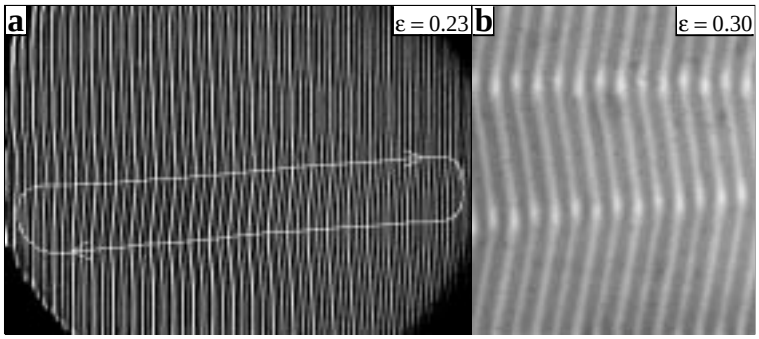

Fig. 7. With 5CB in cell 3 at $h = 1.0$: (a) Typical pattern at the onset of the long-wavelength instability of the normal rolls, in extraordinary light. The curvature lines, which make here an angle of 80° with $\hat{\mathbf{y}}$, disappear at the lateral edges of the cylindrical cell. The white line sketches the possibly associated large scale flows (see text). (b) Zoom on the subsequent zig-zag structure in ordinary light, which gives access to n_z^2.

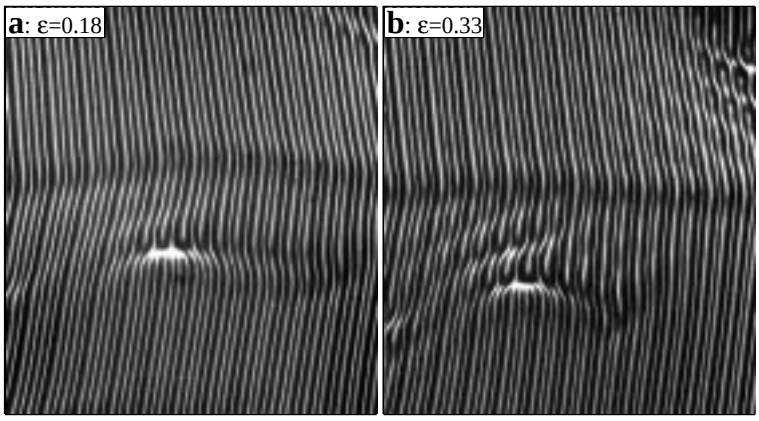

Fig. 8. Nucleation effects in the core of oblique roll dislocations, with 5CB in cell 3 at $h = 0.75$. The images show, in extraordinary light, a zig (top) and a zag (bottom) domains separated by a domain wall. (a) At low ϵ, a small lens of zig nucleates to the right of the core of the dislocation of zag present in the bottom part of the cell. (b) At higher ϵ, the bimodal varicose nucleates around the same dislocation. On the top right of the image there is a portion of the symmetric deformation field of a dislocation of zag (the core of this dislocation is out of frame).

this even provides a new method of measurement of the coherence length ξ_{yy}, according to:

$$\tau_{UR} = \frac{\tau(h)}{\xi_{yy}^2(h)\ p^2} \implies \xi_{yy}(h) = \frac{1}{p}\sqrt{\frac{\tau(h)}{\tau_{UR}}}\ . \qquad (3.3)$$

As shown in Section 5 of [1] , τ_{UR} is expected to reach very large values at $h = 0$, where $\tau(h)$ is the largest. Experimentally, we observe *at small magnetic fields* $h \lesssim 1$ the same type of dynamics as in Figures 5a, b, c after a step to above threshold, but then the system stays in an undulated state for very long times. We estimate for 5CB at $h = 1$, after another relaxation process of 10 days, that $\xi_{yy}(h)$, which is predicted by the linear theory to stay constantly equal to 0.46 for $h \leq 1.4$, in fact decays slightly around $h = 1$, downto values ≤ 0.40. The coherence length $\xi_{yy}(h)$ could even decay more at lower h, but then the τ_{UR} are too long to be measured. Thus at low h a tendency towards *oblique rolls* (OR), of wavevector $\mathbf{q} = q\hat{\mathbf{x}} + p\hat{\mathbf{y}}$ with $p \neq 0$, as in the two modulation modes in (3.2), exists. This tendency is confirmed by the fact that our measured values of q_c are systematically smaller than the ones predicted by the linear theory (Fig. 3). In effect, if one approaches a *Lifshitz point* NR → OR, where $\xi_{yy}(h)$ vanishes, $q_c(h)$ should then strongly decrease: see *e.g.* the limit $h \to 36^-$ in Figure 1a of [2].

We note finally that if at very low h a Lifshitz point existed, higher order terms would have to be included in the development of $\epsilon_0(\mathbf{q}_0 + p\hat{\mathbf{y}})$ in equation (5.5) of [1], and the UR relaxation times would now become

$$\tau_{UR} = \frac{\tau(h)}{\xi_{yy}^2(h)\ p^2 + \xi_{yyyy}^4(h)\ p^4}.$$

The linear theory gives for 5CB, at $h = 0$, $\xi_{yyyy}^4 \simeq 0.39$ *versus* 0.22 for ξ_{yy}^2. So in our cases, for the small p of UR ($p \lesssim 0.2$), the term in p^4 should be at most of the order of a few percent of the term in p^2. If the term in p^4 would only be there, *i.e.* if we assume a Lifshitz point at $h = 0$ for instance, the situation regarding UR would be singular. Then the lateral phase diffusion time in the y direction would scale in Γ^4, giving, for cell 3, $\max \tau_{UR} = \tau(0)/(\xi_{yyyy}^4(0)\ \delta q^4) \simeq 40$ years. Thus the τ_{UR} nearly diverge to the right of a Lifshitz point, whereas to its left UR are known to be possibly metastable [10]. This renders quite difficult the study of the existence of a Lifshitz point in thermoconvection at low h. In fact, the existence of a Lifshitz point around $h \simeq 0.5$ was suggested by earlier experiments with MBBA [11]. Further experimental studies, probably easier in cells of smaller aspect ratio where the phase-diffusion times are smaller ($\Gamma \simeq 20$ should be a good compromise), would be needed to conclude on this point.

4 Cascade of structures

When ϵ is adiabatically increased in the nonlinear regime, in a first range $0 < \epsilon \lesssim \epsilon_{HOPF}$ that will be defined hereafter, we observe a cascade of transitions between *quasi-stationary structures.*

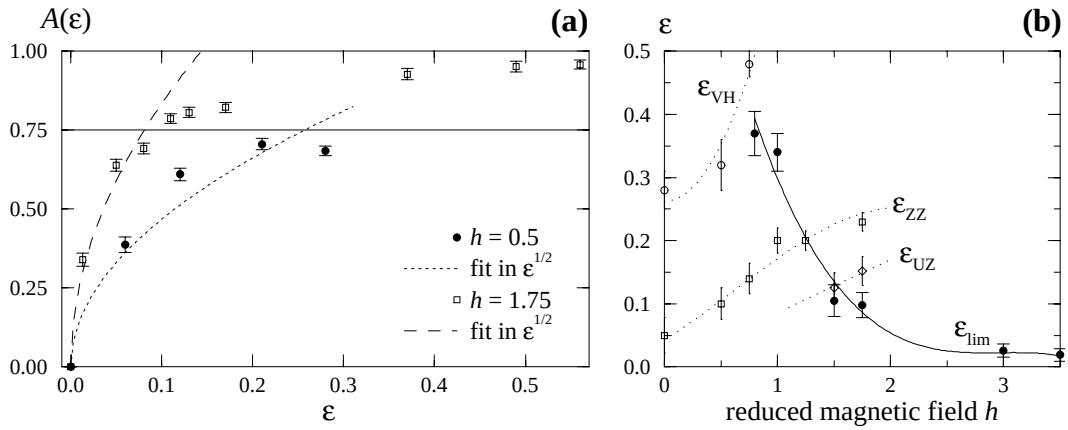

Fig. 9. (a) Typical evolution of the amplitude A of the n_z distortion (3.1) in roll structures. In the weakly nonlinear domain $A(\epsilon) < 0.75$, $\epsilon < \epsilon_{lim}$, fits of the form $A(\epsilon) = Z_{1c}\sqrt{\epsilon}$ shown in dotted ($h = 0.5$) and dashed lines ($h = 1.75$) are consistent with the experimental data. (b) Experimental limit ϵ_{lim} of the weakly nonlinear domain $A(\epsilon) < 0.75$ (filled circles). Also plotted are the thresholds ϵ_{UZ} of the undulation-zig-zag instability (white diamonds), ϵ_{ZZ} of the zig-zag structures (white squares), ϵ_{VH} of the bimodal varicose (white circles). The lines are guides for the eye.

4.1 Transition to zig-zags

Starting at high h with NR, we observe during the ϵ-ramps that some undulations become visible when ϵ is of the order of a secondary threshold ϵ_{UZ}. This corresponds to a continuous spreading of the main Fourier spot in the $\hat{\mathbf{y}}$ direction, which can be quantified as follows. We define the extension of the Fourier spots along $\hat{\mathbf{x}}$ and $\hat{\mathbf{y}}$ respectively as:

$$\Delta q = \sqrt{\langle (q - \langle q \rangle)^2 \rangle} \ ,$$
$$\Delta p = \sqrt{\langle (p - \langle p \rangle)^2 \rangle}$$

where the average designates as usual an integral weighted by the square of the Fourier intensity; another discrete average on the harmonics of the basic mode is also used for a better precision. The ratio $e(\epsilon) = \Delta q(\epsilon)/\Delta p(\epsilon)$ can then be monitored as a function of ϵ. Typically, in a first low ϵ range, we observe that $e(\epsilon)$ fluctuates around an average value: *e.g.* $e(\epsilon) \simeq 1.1 \pm 0.2$ for one set of measurement in 5CB at $h = 1.5$ (and in cell 3). The fluctuations indicate no clear tendency, and the pattern in real space corresponds to "almost perfect" NR. Then, there is a second range in ϵ where a steep increase of $e(\epsilon)$ occurs. For instance, for the measurements in 5CB at $h = 1.5$, $e(0.13) \simeq 1.3$, $e(0.17) \simeq 2.4$, $e(0.24) \simeq 3.0$. This corresponds in real space to the development of the undulations, and the threshold ϵ_{UZ} can be defined as the crossover between these two regimes. After this bifurcation, the model (3.2) (with a non-decaying $a(t)$) must now be used to describe the structures in the homogeneous ideal case. This bifurcation corresponds to a long-wavelength *zig-zag instability* of the NR; *"undulation zig-zag instability"* would in fact be a better name to describe the pattern obtained at onset.

The thresholds ϵ_{UZ} (Fig. 9b) decrease with decreasing h. Starting the ϵ-ramp at small h with UR (Fig. 6a), we observe that when ϵ becomes of the order of ϵ_{UZ}, the undulations already present at threshold start to amplify, and often that new undulations are created, but two regimes can hardly be defined from the study of the extension of the Fourier spots $e(\epsilon)$. On the one hand our finite ϵ resolution renders it difficult to measure several $e(\epsilon)$ values before reaching strongly UR, and on the other hand the measured values show an increase with ϵ beginning roughly at the first threshold. Thus in the low h region a secondary threshold ϵ_{UZ} is difficult to define.

The thresholds ϵ_{UZ} (Fig. 9b) are of the order of the secondary thresholds predicted in [2], but we find a different symmetry of the modulation wavevector $\mathbf{s}$. In [2], the bifurcation was rather predicted to be of the "skewed varicose type", *i.e.* with an angle arg($\mathbf{s}$) between $\hat{\mathbf{x}}$ and $\mathbf{s}$ of the order of 45° instead of 90°. Recent calculations would show that the weakly nonlinear theory is insufficient to predict the bifurcation type [12]. We, in fact, observed in some experiments an initial angle arg($\mathbf{s}$), which is also the angle between the curvature lines associated with the undulations and $\hat{\mathbf{y}}$ [1], of 80° instead of 90° (Fig. 7a). Thus a slightly skewed long-wavelength instability cannot be excluded. In Figure 7a, where the major part of cell 3 is visible, we can also observe some finite size effects on the long-wavelength instability. A loop of curvature is visible, which avoids the lateral walls of the cell. It suggests that *large scale horizontal flows*, sketched in Figure 7a, and which should avoid the lateral walls, could play an active role in the instability as predicted in [13] for the case of electroconvection. To evaluate this possibility, we made some preliminary studies of the trajectories of dust particles in the structures. We tracked the particles using a microscope objective, but the large thicknesses of the cells rendered the observations difficult, whereas on the other hand the periods were very long (typically 90 minutes, a time related to the low values of the velocity amplitudes

[1] Indeed (3.2) gives $n_z(\mathbf{r}) = A\sin(q_c x) + 2a\cos(q_c x)\sin(\mathbf{s}\cdot\mathbf{r})$, from which the curvature lines appear to be the locus of the points where $\mathbf{s}\cdot\mathbf{r} = (n + 1/2)\pi$.

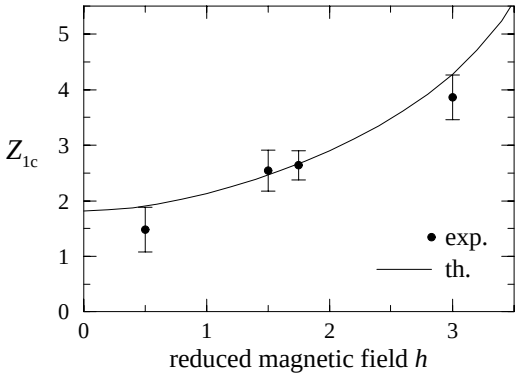

Fig. 10. Values of $Z_{1c}(h)$ deduced from the fits of $A(\epsilon)$ in the weakly nonlinear domain as in Figure 9a. They are consistent with the predictions of the weakly nonlinear theory (see text).

calculated in equation (4.13) of [1]). Thus we could not reach to a definitive conclusion about this point.

When ϵ is further increased, the undulations straighten and form acute angles. This straightening corresponds to the development of higher harmonics ($\mathbf{s}' = m\mathbf{s}$) of the initial modulation wavevector $\mathbf{s}$, and indeed the extension of the main Fourier spot along $\hat{\mathbf{y}}$ increases. Naming $\mathbf{s}'$ the modulation wavevector which presents the maximal Fourier intensity, we observe the existence of a rather reproducible ϵ threshold where $\mathbf{s}'$ and its symmetric under S: $\hat{\mathbf{y}} \mapsto -\hat{\mathbf{y}}$ get far enough such that the main Fourier spot splits into two spots. This splitting can be defined by monitoring the Fourier intensity $I_q(\epsilon)$ along the axis $p = 0$, which decays steeply downto a noise value when it occurs. One Fourier spot is then centered around

$$\mathbf{q} = \mathbf{q}_0 + \mathbf{s}' = |\mathbf{q}|(\hat{\mathbf{x}}\cos\theta + \hat{\mathbf{y}}\sin\theta) \quad \text{with} \quad \theta > 0 \quad (4.1)$$

for the "zig", and the other around $S(\mathbf{q}) = \mathbf{q}_0 + S(\mathbf{s}')$ for the "zag" (Fig. 6b). This splitting defines a threshold of *zig-zag structures* ϵ_{ZZ}, for which we find experimentally that $\theta \simeq 4°$. The reflection S is a global symmetry of the system, which has been broken in the whole transition process from NR to these zig-zag structures, through the intermediary undulated roll state. Indeed one observes in real space the coexistence of domains with the zig or the zag wavevector, separated by curvature lines, which are domain walls. These zig-zag structures persist over very long times ($\gtrsim 30\ \delta t$), with only very slow displacements of the domain walls (by typically one roll spacing over δt): the selected OR of wavevector $\mathbf{q}$ and $S(\mathbf{q})$ may be regarded as stable, in contradiction with the weakly nonlinear theory [2], but in agreement with recent fully nonlinear calculations [12]. We never observed an evolution to a monodomain either zig or zag (over times up to 30 δt). In ordinary light, the OR appear just like tilted NR: see Figure 7b, where the intensity profiles perpendicularly to the rolls are in $\sin^2 \mathbf{q}\cdot\mathbf{r}$ as for NR. Thus the n_z distortion in zig-zag structures can be approximated by

$$n_z(\mathbf{r}) = A(\mathbf{r})\ \sin\mathbf{q}\cdot\mathbf{r}\ +\ B(\mathbf{r})\ \sin S(\mathbf{q})\cdot\mathbf{r}. \quad (4.2)$$

In a zig domain for instance, $B = 0$, and the constant value of A is determined only by the values of the wavevector $\mathbf{q}$ and ϵ, as will be shown in the next subsection. We have also introduced in (4.2) amplitudes depending on $\mathbf{r}$, in order to allow for the description of inhomogeneous structures. For instance, a nucleation effect occurs in the core of OR dislocations, as shown in Figure 8a. A lens of the zig nucleates inside a dislocation of zag (and *vice versa*). The lens of zig tends to be static, *i.e.* not to grow. This effect can be interpreted by the fact that in the core of a defect of zag, the zag amplitude is weaker, and consequently the damping of the zig by nonlinear competition with the zag is weaker. Since the zig is linearly excited, it can thus develop in a small region around the core of the zag dislocation. This is found from the lowest-order coupled amplitude equations model provided that the nonlinear competition coefficient g_2 between zig and zag is not too strong (Sect. 6 of [1]). Also, the fact that locally in the domain walls between zig and zags the amplitude $n_z(\mathbf{r})$ is higher (Fig. 7b) can be accounted for by the model (Eq. (6.3) of [1]), under the condition $g_2 < 3$. This can be shown by numerical simulations of equation (6.3) of [1] connecting zig and zag domains through a wall parallel to $\hat{\mathbf{x}}$. Then the amplitudes A and B depend only on y. For $g_2 < 3$, the zig and zag amplitudes intersect at $|A|, |B| > 0.5\sqrt{\epsilon}$, implying a local peak of n_z (4.2) inside the wall, whereas, for $g_2 > 3$, they intersect at $|A|, |B| = 0.5\sqrt{\epsilon}$, and there is no peak of n_z inside the wall. Similar effects concerning domain walls were in fact reported in [14], but without precise definitions of the limits in the coupling coefficients.

As ϵ is further increased, the wavevector $\mathbf{q}$ of zig rolls, which can still be written under the form (4.1), presents an evolution because of complex long-wavelength selection processes. Both $|\mathbf{s}'|$ and θ increase. Moreover, $\mathbf{s}'$ slightly rotates when ϵ increases, so that the angle $\arg(\mathbf{s}')$ decays to $\simeq 70°$ at higher ϵ. Finally, at the threshold of the homogeneous bimodal varicose (see Sect. 4.3), which is the upper limit of the stable OR domain, $\mathbf{q}$ (4.1) has evolved to $\mathbf{q}_f$ such that, for 5CB,

$$|\mathbf{q}_f|/q_c = 1.07 \pm\ 0.02\ , \quad \theta_f = \arg\mathbf{q}_f = 8° \pm\ 1°. \quad (4.3)$$

For MBBA $|\mathbf{q}_f|/q_c$ is of the same magnitude whereas $\theta_f = 10° \pm\ 2°$.

4.2 Evolution of the main convective amplitude in roll structures

In NR, in UR far from the curvature lines, or in OR far from the domain walls, there exist locally a well-defined wavevector $\mathbf{q}$ and amplitude A such that the n_z distortion reads to lowest order $n_z(\mathbf{r}) = A\sin\mathbf{q}\cdot\mathbf{r}$. In the so-called weakly nonlinear regime, and according to the standard weakly nonlinear theories, homogeneous rolls should be unambiguously characterized by this wavevector and by this amplitude; we therefore name A the "main convective amplitude". From a Fourier transform of the roll patch, we can measure $\mathbf{q}$, and from our optical methods (Eq. (8) in Ref. [6]), we can measure A from the angles of aperture of the caustic cusps. Our finite ϵ resolution, and the fact that

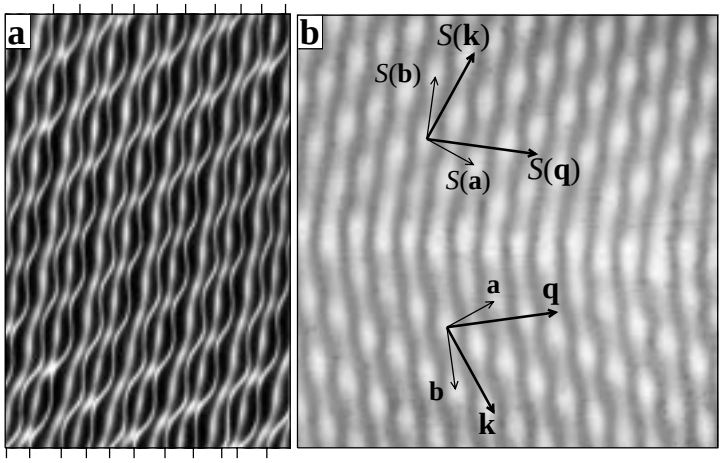

Fig. 11. Bimodal varicose structures. (a) With MBBA in cell 1, at $h = 0.8$, $\epsilon = 0.32$, observed in extraordinary light. As compared with the initial oblique roll structure, the center lines are almost not changed, *i.e.* they remain almost straight. On the other hand, the edge lines (marked by the ticks below and above the image) show a periodic pinching. (b) With 5CB in cell 3, at $h = 1.75$, $\epsilon = 0.69$, observed in ordinary light. The direct lattice basis vectors are shown by the thin lines. The reciprocal lattice basis vectors, which are also the wavevectors of the roll modes in the bimodal, are shown by the thicker lines. In the lower part the bimodal varicose is constructed on the zig $\mathbf{q}$ and its dual $\mathbf{k}$, and in the upper part on the zag $S(\mathbf{q})$ and its dual $S(\mathbf{k})$.

our optical methods are only accurate for not too small A, forbid a study of the bifurcation scenario near the first threshold ($\epsilon = 0$): we can only check that no hysteresis appears within our experimental resolution $\delta\epsilon$. On the other hand, we can measure A during our ramps in ϵ, up to the varicose threshold ϵ_{VH} (see Sect. 4.3), where our method of measurement breaks down. Two series of measurements of $A(\epsilon)$, at representative values of the reduced magnetic field h, are shown in Figure 9a. They are performed in the case of 5CB in cell 3, to which we restrict now.

In order to interpret these measurements, let us first propose a definition of the weakly nonlinear domain. Since the system is in the DDR, a criterion of small amplitude of the director distortion,

$$\epsilon < \epsilon_{lim} \iff A(\epsilon) < 0.75, \tag{4.4}$$

seems reasonable. Experimentally, we could only measure ϵ_{lim} for h values larger than 0.75, because for smaller h the amplitude A does not reach 0.75 before the varicose instability (Fig. 9b). As h is increased, we observe a very strong decrease of ϵ_{lim}. We can relate ϵ_{lim} to the predictions of the weakly nonlinear theory, which give for the amplitude of the n_z distortion (Eq. (4.14) of [1]):

$$A(\epsilon) = Z_1(\mathbf{q}(\epsilon))\ \sqrt{\epsilon}. \tag{4.5}$$

There, the shift $\epsilon_0(\mathbf{q})$ of the threshold for $\mathbf{q} \neq \mathbf{q}_0$ has been neglected since one has always $\epsilon_0(\mathbf{q}) \lesssim 0.015$ which is small as compared with our ϵ resolution. For $h \gtrsim 1.5$, $\mathbf{q}$ does not vary in the weakly nonlinear domain, so $Z_1(\mathbf{q}(\epsilon))$ in (4.5) should be constant, equal to $Z_{1c} := Z_1(q_c\hat{\mathbf{x}})$. On the other hand, for $h \lesssim 1.5$, the transition to zig-zag structures occurs inside the weakly nonlinear domain (Fig. 9b), and simultaneously the wavevector evolves from $q_c\hat{\mathbf{x}}$ to $\mathbf{q}_f$ (4.3) inside this domain. Nevertheless, we checked, with the Galerkin method exposed in Section 4.1 of [1], including 4 vertical modes, that during this evolution $Z_1(\mathbf{q})$ should only slightly decrease, by 9% at $h = 0$, 10% at $h = 0.5$, 13% at $h = 1.5$. Neglecting these rather small corrections, one expects $A(\epsilon) \simeq Z_{1c}\sqrt{\epsilon}$ in the weakly nonlinear domain $A < 0.75$. This is consistent with all our experimental datas, as show for instance the fits in Figure 9a. We can even extract from these fits the values of Z_{1c}, which roughly agree with the predictions of the weakly nonlinear theory (Fig. 10). By comparison of (4.4, 4.5) with equation (4.14) of [1], we obtain

$$\epsilon_{lim} = \frac{9}{16}(Z_{1c})^{-2} = \frac{9}{64}\ \tau\ g_{\mathbf{q}_c}, \tag{4.6}$$

i.e. that ϵ_{lim} measures the nonlinear saturation coefficient $g_{\mathbf{q}_c}$. The decrease of ϵ_{lim} with h appears therefore to be connected with a tendency towards a *subcritical bifurcation* around $h = 4$, which is clear from Figures 9b and 10. The fact that $g_{\mathbf{q}_c}$ should become negative around $h = 4$ was predicted in [2] (see also the end of Sect. 4.2 of [1]). We performed some experiments at $h = 4$, where we may leave the Boussinesq conditions since, at this high magnetic field value, $\Delta T_c \simeq 5.5$ °C. We still found no hysteresis within our experimental resolution. But, surprisingly, we found that $A(\epsilon)$ does not reach 0.75 before we observe, around $\epsilon = 0.04$, some peculiar symmetry breaking on the rolls, where one roll becomes larger and the other one thinner. This effect could be related to a slight tilt of the cell over the horizontal plane, which is somehow amplified at high magnetic field. Further studies with a thicker cell would be needed in this high h region.

Even for $h \lesssim 3.5$, we observed some anomalous behavior in the amplitude variations $A(\epsilon)$ that cannot be explained by the standard weakly nonlinear theory. We systematically found at high ϵ that A almost does not increase (curve $h = 1.75$, Fig. 9a) or can even decrease after a positive ϵ step (last point at $h = 0.5$, Fig. 9a). This can be heuristically understood, at least for the curve at $h = 1.75$, by the fact that the director component n_z is definitely not an extensive physical variable: it should verify $n_z < 1$ from the normalization condition $\mathbf{n}^2 = 1$. Thus it is certain that A should stay smaller than 1, *i.e.* that the structure of the convection rolls *must* change before A reaches 1. What happens is not clear from the optical patterns, which show no special effects when the amplitude plateau or the decrease is observed.

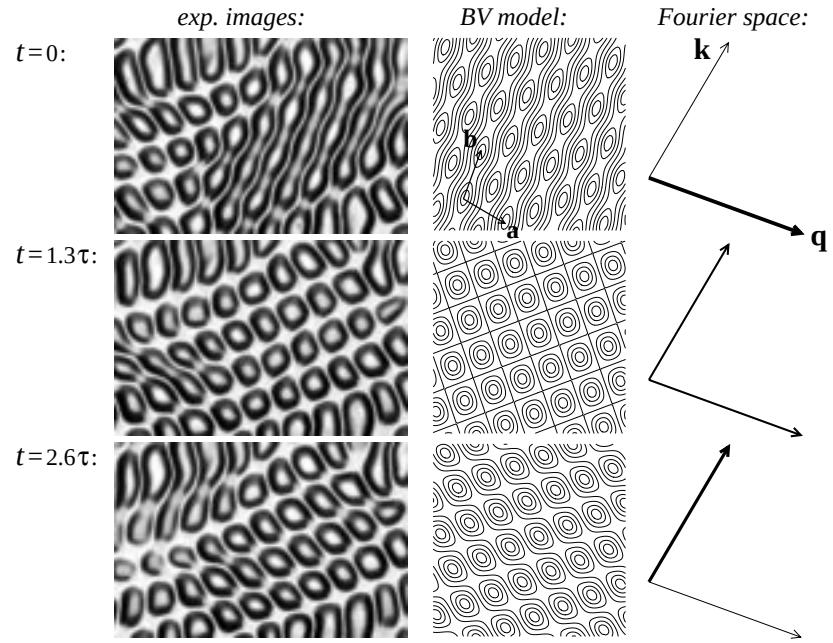

Fig. 12. Oscillations in a bimodal varicose structure, of the zag type, with MBBA in cell 3 at $h = 0, \epsilon = 0.5$. Here one half period of oscillations is shown. The left column shows three experimental images (in extraordinary light) of the same portion of the cell (of width $\simeq 10$ rolls), separated by an interval of $1.3\ \tau(h) = 30$ min. The middle column shows a numerical reconstitution of the level lines of $n_z^2(\mathbf{r})$, with the bimodal varicose (BV) model $n_z(\mathbf{r}) = A\sin(\mathbf{q}\cdot\mathbf{r}) + B\sin(\mathbf{k}\cdot\mathbf{r})$ (4.7). The basis wavevectors $\mathbf{q}$ and $\mathbf{k}$ are shown in the last column, whereas the direct lattice basis vectors $\mathbf{a}$ and $\mathbf{b}$ are shown on the first image of the second column. A good reconstitution of the right part of the pattern is observed. From the top to the down row, we used $B/A \simeq 0.25,\ 1,\ 1.6$ respectively. We sketched these amplitude oscillations by varying correspondingly the thickness of the wavevectors in the last column.

4.3 Transition to bimodal varicose

In the absence of any defect, a oblique roll domain undergoes, when ϵ gets larger than a threshold ϵ_{VH}, a new bifurcation characterized in extraordinary light by the development of a pinching of the edge lines of the rolls with a secondary period (Fig. 11a). The resulting structure, which was first found in electroconvection [15], has been called varicose by analogy with similar patterns found in Rayleigh-Bénard convection [16]. The "VH" in ϵ_{VH} stands thus for "varicose, homogeneous". In ordinary light (Fig. 11b), we checked that the n_z field of this structure can be written as the superposition:

$$n_z(\mathbf{r}) = A\ \sin\mathbf{q}\cdot\mathbf{r}\ +\ B\ \sin\mathbf{k}\cdot\mathbf{r} \qquad (4.7)$$

where A and B are resp. amplitudes. This proves that this structure is a bimodal, and, in order to avoid possible confusions with the long-wavelength skewed-varicose structure, described rather by a "trimodal" of the type (3.2), we name it the *bimodal varicose*. The geometrical appearance of the bimodal varicose in extraordinary light can also be understood from (4.7), assuming that the edge lines are given by the locus of the points where $n_z(\mathbf{r}) = 0$. This is reasonable since above these lines the rays are not deflected. The "pinching", defined as the maximum distance l between the new edge lines and the former ones (when B was equal to 0), can be deduced as $l = |\mathbf{a}|/(2\pi)\arcsin(B/A)$, where $\mathbf{a}$ is the direct lattice basis vector reciprocal to $\mathbf{q}$ (Fig. 11b). Since the pinching l increases smoothly with ϵ, the transition to homogeneous bimodal varicose seems to be a forward bifurcation, as it was observed in electroconvection (where $l(\epsilon)$ has been accurately measured, see Fig. 2 of [15]). Finally, the bimodal model can be confirmed by studies of the trajectories of particles, and comparison with numerical simulations of these trajectories assuming a bimodal velocity field (Appendix A).

In (4.7), $\mathbf{k}$ is a new wavevector named the *dual* of $\mathbf{q}$, since it should depend unambiguously of $\mathbf{q}$ [5]. We measured for MBBA and 5CB, $0 \le h \le 2$, and at ϵ_{VH}, that the variant of bimodal varicose constructed on the zig has a first wavevector given by (4.1, 4.3) and a dual wavevector:

$$\mathbf{k} = |\mathbf{k}|(\hat{\mathbf{x}}\cos\phi + \hat{\mathbf{y}}\sin\phi)$$
$$\text{with}\ \ |\mathbf{k}|/|\mathbf{q}| = 0.9 \pm\ 0.05,\ \ \phi = -55^\circ \pm\ 5^\circ. \qquad (4.8)$$

The transition to bimodal varicose is qualitatively well described by the weakly nonlinear model developed in Section 7 of [1]: the dual mode deduced from the model is found in the zag region, far from the zag; the increase of ϵ_{VH} ($= \epsilon_V$ in [1]) with h at very low h is found; the law $B/A \propto \sqrt{\epsilon - \epsilon_{VH}}$ can be derived. Nevertheless, the theoretical values of $\phi = \arg\mathbf{k}$ and of the threshold ϵ_{VH} are too small (by a factor of $\simeq 0.6$ at $h = 0$), presumably because of higher order effects not included in the weakly nonlinear analysis.

An interesting aspect of the transition to bimodal varicose is that, whenever a defect is present in an oblique roll structure, it always nucleates the bimodal, as soon as ϵ gets larger than a critical threshold ϵ_{VL} (L stands for a "localized" varicose). In Figure 8b one sees a bimodal varicose lens close to the core of an oblique-rolls dislocation, in a specific region which depends only on the topological charge of the dislocation. The second period is the same as in the bimodal varicose, but the amplitude of the pinching decreases strongly outside of the core of the dislocation. The lens is static, *i.e.* its area grows only when ϵ is further increased. These pretransitional localized effects are probably linked to localized nonlinear competition effects analogous to the one studied in Section 6 of [1], but not to a subcritical bifurcation. Indeed it is known that, even if a secondary bifurcation is supercritical in the homogeneous case, the nonlinear competition in defects of the

primary structure can lead to a localized nucleation of the bifurcated structure (this was shown for instance for the pairing process in mixing layers [17]; see also the conclusion of [1]). Note finally that, as for the zig-zag structures, the bimodal varicose structures never evolve to a monodomain: one observes, as in Figure 11b, several domains where the primary wavevector in the bimodal is either zig or zag.

5 Oscillations in bimodal structures

When ϵ is adiabatically increased above ϵ_{VH}, in a first ϵ domain $\epsilon_{VH} < \epsilon < \epsilon_{HOPF}$, the only effect is an increase of B/A, *i.e.* of the pinching l in the bimodal varicose domains. The pattern remains quasi-stationary, except for the very slow dynamics of the domain walls. This stationarity breaks down at higher ϵ. Indeed, after some step of ϵ, around a "threshold" value ϵ_{HOPF} which seems to depend on the precise pattern in the cell, some oscillations appear inside the bimodal varicose domains. This can be seen in Figure 12, which shows the time evolution of a bimodal varicose zag domain at fixed $\epsilon > \epsilon_{HOPF}$. In the whole area imaged, the bimodal varicose is based on the zag $\mathbf{q}$ and its dual $\mathbf{k}$, and can be well reconstructed by the model (4.7), but with amplitudes A and B now depending on the time t and the position $\mathbf{r}$. The dependence on t consists in a periodic switching between the primary roll mode in the bimodal and its dual roll mode: $B/A(t)$ oscillates, with a period $T \simeq 5.2\tau = 2$ h in the case of Figure 12. Indeed, in the right part of the image, one can see from the numerical reconstitution of columns 2 and 3 of Figure 12 that: at $t = 0$, $B/A \simeq 0.25$, the zag rolls dominate and are slightly modulated by the dual rolls; at $t = 1.3\tau = T/4$, $B/A \simeq 1$, the superposition of the two modes with the same power leads to a bimodal with closed cells; at $t = 2.6\tau = T/2$, $B/A \simeq 1.6$, the dual rolls dominate and are slightly modulated by the zag rolls. Of course at $t = 3T/4$, the pattern obtained is the same as the one at $t = T/4$, and so on. There is also a space−dependence (in $\mathbf{r}$) of the phase of this oscillation, such that in Figure 12 for instance the left part of the pattern oscillates in advance as compared with the right part, the delay being of the order of 1.3τ. Indeed at $t = 1.3\tau$ one can observe on the left of the image dual rolls which appear on the right of the image only at $t = 2.6\tau$. Finally, we observe that the amplitude of the oscillations is also not homogeneous in space. In some experiments we even observe, close to ϵ_{HOPF}, that the oscillations develop only in some areas of the cells, whereas in other areas the bimodals stay stationary. Consequently, a general model for oscillations in a bimodal varicose domain would be in a first approach:

$$
\begin{aligned}
n_z(\mathbf{r},t) &= A(\mathbf{r},t)\ \sin\mathbf{q}\cdot\mathbf{r}\ +\ B(\mathbf{r},t)\ \sin\mathbf{k}\cdot\mathbf{r} \\
\text{with}\quad A(\mathbf{r},t) &\simeq A_0\Big(1+a(\mathbf{r})\cos(\omega t+\phi(\mathbf{r}))\Big), \\
B(\mathbf{r},t) &\simeq B_0\Big(1-b(\mathbf{r})\cos(\omega t+\phi(\mathbf{r}))\Big) \qquad (5.1)
\end{aligned}
$$

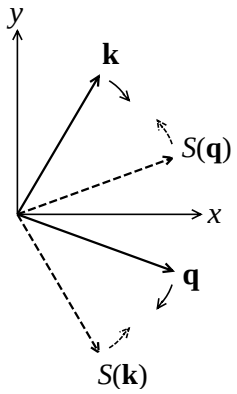

Fig. 13. Representation of the evolution, with increasing ϵ, of the basic wavevectors in the bimodal varicose. There exists a threshold ϵ_{SYM} where $\mathbf{q}$ and $S(\mathbf{k})$, $\mathbf{k}$ and $S(\mathbf{q})$ come to coincide. The bimodals then become *symmetric*.

where $\omega = 2\pi/T$. The spatial variations of the amplitudes a, b and the phase ϕ appear to depend strongly on the location of the domain walls between zig and zag bimodals, and on the presence of point defects. We never observed a total phase coherence: the oscillations were never homogeneous in space, even inside a single bimodal domain without defects. This is for instance the case in Figure 12, where no defect separates the left from the right part of the pattern. Nevertheless, a careful examination of the patterns in Figure 12 shows that the bimodal varicose structure is not perfect, in that the underlying lattice presents some distortions: a curvature of the lines parallel to the sum of the direct lattice vectors $\mathbf{a}+\mathbf{b}$ is visible. This distortion of the bimodal lattice could be modeled by introducing in (5.1) a $\mathbf{r}-$dependence of the wavevectors $\mathbf{q}$ and $\mathbf{k}$. It is then reasonable to assume that these distortions of the bimodal structure couple to the phase of the oscillations, and are partly responsible for the phase inhomogeneities.

When ϵ is increased above ϵ_{HOPF} , the number of domains of oscillating bimodal varicose based on either zig or zag increases, together with the number of point defects. Thus, a pattern of rather high spatio-temporal complexity is obtained, with smaller and smaller domains. The direct calculation of the reciprocal lattices of these oscillating bimodal varicose structures shows that the underlying wavevectors $\mathbf{q}$ and $\mathbf{k}$ rotate with increasing ϵ: $\mathbf{q}$ goes away from the x axis, whereas $\mathbf{k}$ comes closer to the x axis (Fig. 13). There exists therefore a last "threshold" ϵ_{SYM} where $\mathbf{q}$ comes to coincide with $S(\mathbf{k})$ and $\mathbf{k}$ comes to coincide with $S(\mathbf{q})$. Above this threshold, the oscillations occur now in symmetric bimodals, as shown in Figure 14. Note that the rotation of the wavevectors sketched in Figure 13 is not rigid. Typically $\arg\mathbf{k}$ decreases from roughly 55° at ϵ_{VH} to roughly 30° at ϵ_{SYM}, whereas $\arg\mathbf{q}$ decreases from roughly −8° at ϵ_{VH} to roughly −30° at ϵ_{SYM}. Finally, this wavevector evolution might be discontinuous, since the last transition from unsymmetric to symmetric oscillating bimodals is spatially inhomogeneous: thus the coincidence of all wavevectors could be associated with a subcritical bifurcation.

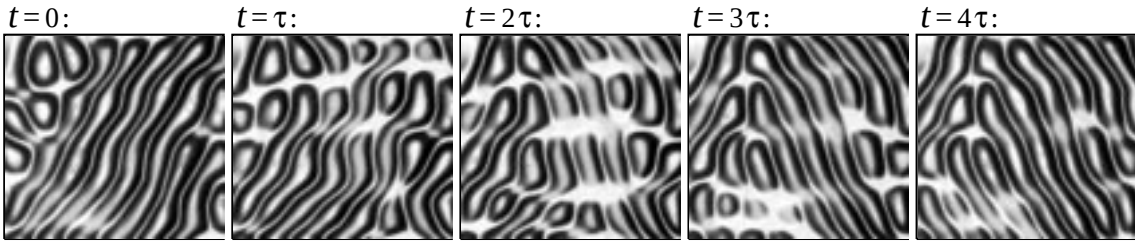

Fig. 14. Half period of oscillations in a symmetric bimodal structure, with MBBA in cell 3 at $h = 0, \epsilon = 1.4$. The images are separated by an interval of $\tau(h) = 22.5$ min. In the first image, at $t = 0$, the zag rolls dominate, whereas in the last image, at $t = 4\tau = T/2$, the zig rolls dominate.

The transition towards a symmetric bimodal state occurs far above the onset of the bimodal oscillations only for MBBA, where ϵ_{SYM} indeed appears to be larger than ϵ_{HOPF}: at $h = 0$, we measured $\epsilon_{HOPF} = 0.5 \pm 0.12$, $\epsilon_{SYM} = 1.3 \pm 0.3$. In 5CB, the situation turns out to be more intricate, since we found, at $h = 0$, $\epsilon_{SYM} \simeq \epsilon_{HOPF} = 0.7 \pm 0.12$: in some experiments the bimodals become symmetric inside the stationary range, and in other experiments the oscillations develop in unsymmetric bimodals before the coincidence of the zag and the zig dual. Also, in 5CB, the oscillations are more localized than in MBBA, and very often the coexistence of stationary and oscillating patches is observed. This may be due to differences in the material parameters of MBBA and 5CB: in this highly nonlinear regime, the bifurcation thresholds are probably very sensitive to small differences in these parameters. Note finally that the oscillations apparently present a large but finite period at ϵ_{HOPF}, and that this period T slightly increases with increasing ϵ. For instance for MBBA at $h = 0$, $T/\tau = 5.5 \pm 0.5$ at ϵ_{HOPF}, $T/\tau = 8 \pm 0.5$ at ϵ_{SYM} ; for 5CB at $h = 0$, $T/\tau = 15 \pm 0.7$ at $\epsilon_{HOPF} \simeq \epsilon_{SYM}$.

Bifurcations towards oscillating bimodal states have been evidenced experimentally long ago in electroconvection [18,19]. These papers have described the symmetric bimodal case, but recently oscillations in a unsymmetric bimodal varicose have also been reported [20]. Therefore the last two steps analyzed in this Section seem to be generic for planar nematic convection. Note also that a coupling between distortions of the bimodal lattice and the oscillations has been evidenced in [21]. In this case the bimodal was symmetric, and only Eckhauss-like distortions appeared to be important. In our case, the curvature of the bimodal seems to play also an important role.

6 Conclusion

The transition towards spatio-temporal complexity in planar nematic thermoconvection in the director-dominated regime develops, as the control parameter ΔT is increased, through a *cascade of spatio-temporal structures*. The first part of this cascade, at rather low ΔT, consists in a sequence of quasi-stationary structures:

normal rolls
↓
undulated rolls
↓
oblique rolls
↓
bimodal varicose.

The very long characteristic times at low magnetic field h render the separation between transient and (meta)stable undulated rolls almost impossible, so that a clear definition of the first step of the cascade at low h is difficult to give. Correlatively, the very slow dynamics of the curvature lines in the undulated rolls, or of the domain walls in the oblique rolls and the bimodal varicose, induces a very slow time-dependence. At higher ΔT, a Hopf bifurcation is observed, together with an evolution of the wavevectors in the bimodal varicose:

(quasi stationary) bimodal varicose
↓
oscillating bimodal varicose
↓
oscillating symmetric bimodal.

These two last bifurcations are inhomogeneous and "pattern-dependent".

We have given the measurements of the thresholds ϵ_{UZ}, ϵ_{ZZ} and ϵ_{VH} of the bifurcations towards undulated rolls, zig-zags (= oblique rolls) and bimodal varicose for 5CB in [5]. On the other hand, the "thresholds" ϵ_{HOPF} and ϵ_{SYM} of the bifurcations towards oscillating bimodals and symmetric bimodals are not as clearly defined. Also, it must be noted that up to now no theoretical explanation of these highly nonlinear oscillating regimes exist. Therefore, we will conclude this article by giving a *tentative* diagram of bifurcations only (Fig. 15), which mainly relies on the results obtained for MBBA (the diagram for 5CB is analogous, except for the fact that the lines ϵ_{HOPF} and ϵ_{SYM} are very close). This tentative diagram Figure 15 is similar to the diagram evidenced in planar nematic electroconvection at low frequency [20]. This proves that the cascade of spatio-temporal structures presented here is *generic* for planar nematic convection in the director-dominated regime, *i.e.* independent of the basic

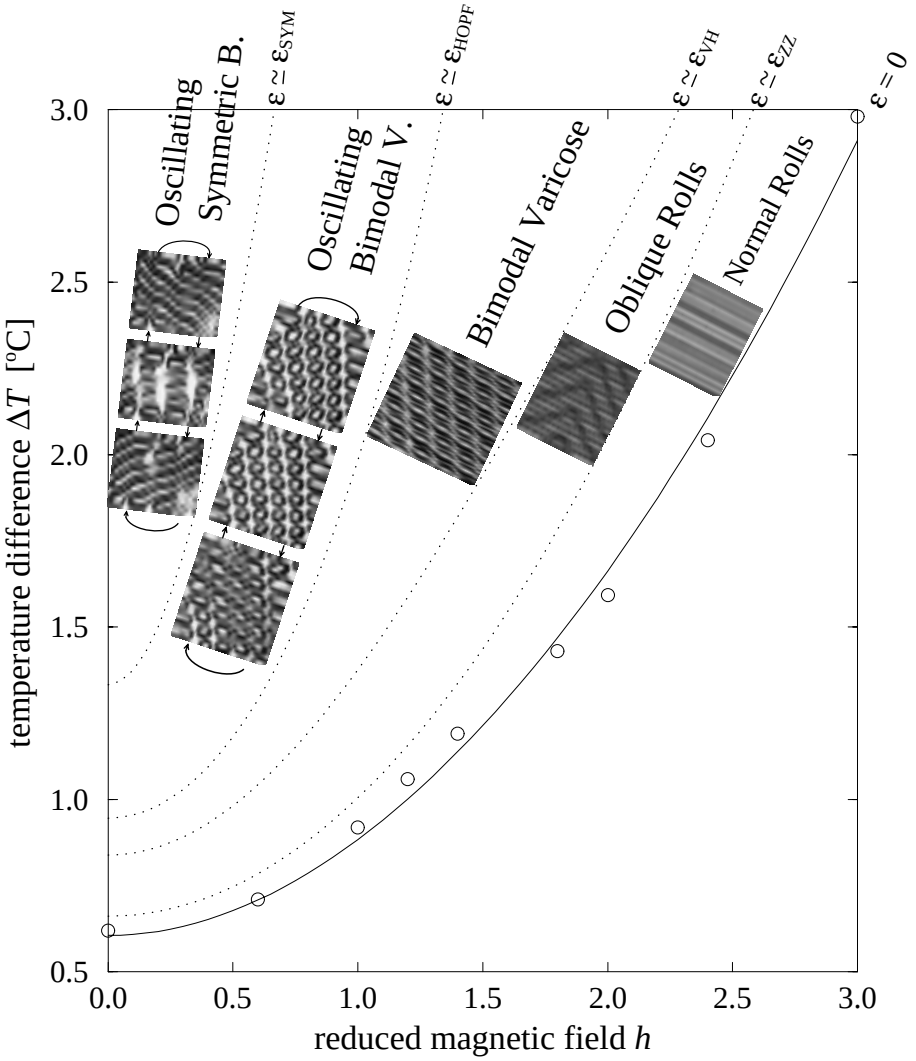

Fig. 15. Tentative diagram of bifurcations for MBBA in cell 3. The open circles show the experimental measurements of the convection threshold. The continuous line $\epsilon = 0$ is the theoretical convection threshold obtained after fitting of the thermal expansion coefficient α (see Sect. 3). The dotted lines shown are only reasonable guesses for the other bifurcation "lines" in the nonlinear regime. Indeed, the experimental uncertainties on the position of these lines increase strongly with the order of the bifurcation: whereas the uncertainties on the first threshold ($\epsilon = 0$) were only of $\pm$ 0.05 °C, the last line ($\epsilon \simeq \epsilon_{SYM}$) is only determined to a precision of $\pm$ 0.2 °C. We had no room to show the undulated rolls domain, which consists in a narrow band of width $\simeq$ 0.1 °C below the line $\epsilon \simeq \epsilon_{ZZ}$.

convective mechanism. In particular, the existence of the oscillations in thermoconvection proves that they do not originate from ac effects, as was (erroneously) speculated in electroconvection. This conclusion should motivate new theoretical works addressing, from the basic nematohydrodynamic equations, the modeling of the Hopf bifurcation in bimodal structures.

The simplicity of the basic structures identified here above should not hide the fact that the real patterns are always inhomogeneous in space, and that a rather complex spatio-temporal dynamics results from this inhomogeneity. For instance some nucleation effects are associated with the point-defects, and the coupling between the bimodal distortions and the phase dynamics of the oscillations in the last structures apparently entails new effects that remain to be studied.

Finally, it seems now important to develop optical techniques that could allow for the observation of the n_y distortion. In effect, the techniques that we have used are rather insensitive to n_y [6] because of the Mauguin principle of adiabatic rotation of light polarization [22]. We plan new experiments in this direction, which could test the structure of the homogeneous n_y field in oblique rolls predicted in [1].

We thank A. Belaidi for discussions about experiments in electroconvection. This work was supported by the Direction des Recherches et Études Techniques under contract DGA/DRET/94136.

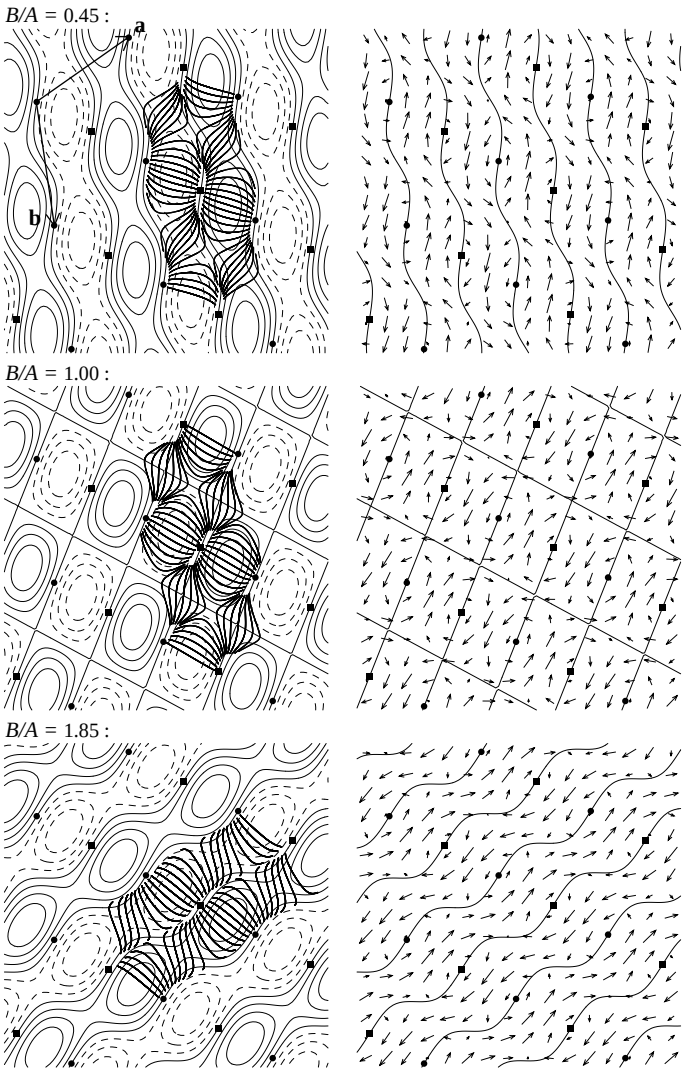

Fig. 16. Flow structure and out-of-plane director field in the bimodal varicose, as predicted from the lowest-order theoretical model. For increasing values of the ratio B/A of the amplitudes of the zig and its dual, the left column shows: with the black circles (squares), the maxima (minima) of the temperature field (A.2); with the continuous (dashed) thin lines, the level lines of the n_z field (A.1) for positive (negative) isovalues; with the thick lines, some fluid trajectories. On the first image $B/A = 0.45$, the direct lattice basis vectors **a** and **b** are shown. The right column shows again the maxima and minima of temperature, together with the lines $n_z(\mathbf{r}) = 0$. It also shows with the arrows the horizontal vorticity in the mid-plane of the layer (A.5).

Appendix A: Fluid trajectories in the bimodal varicose

In this appendix, we present a theoretical characterization of the local fields in the bimodal varicose, and more specifically a Lagrangian description of the velocity field. We will compare with experimental observations of the trajectories in the bimodal varicose in electroconvection [15], where these observations are more easy to perform than in thermoconvection (see the discussion of Sect. 4.1). In order to be coherent with the phase choice made in Section 3 of [1], we define now the amplitudes in the bimodal varicose by

$$n_z(\mathbf{r}) = -(A\ \sin \mathbf{q}\cdot\mathbf{r}\ +\ B\ \sin \mathbf{k}\cdot\mathbf{r}), \tag{A.1}$$

where we assume $A, B \geq 0$. We also introduce $A_\theta = \tilde{\theta}(\mathbf{q})/|\tilde{n}_z(\mathbf{q})|\ A$, $B_\theta = \tilde{\theta}(\mathbf{k})/|\tilde{n}_z(\mathbf{k})|\ B$, $A_f = \tilde{f}(\mathbf{q})/|\tilde{n}_z(\mathbf{q})|\ A$, $B_f = \tilde{f}(\mathbf{k})/|\tilde{n}_z(\mathbf{k})|\ B$. Because of the form equation (3.2) of [1] of the linear roll modes, the temperature, horizontal and vertical velocity fields should be to leading order

$$\theta(\mathbf{r}, z) = (A_\theta\ \cos \mathbf{q}\cdot\mathbf{r}\ +\ B_\theta\ \cos \mathbf{k}\cdot\mathbf{r})\ S_1(z), \tag{A.2}$$

$$\mathbf{v}_h(\mathbf{r}, z) = -(A_f\ \mathbf{q}\ \sin \mathbf{q}\cdot\mathbf{r}\ +\ B_f\ \mathbf{k}\ \sin \mathbf{k}\cdot\mathbf{r})\ C_1'(z), \tag{A.3}$$

$$v_z(\mathbf{r}, z) = (A_f\ \mathbf{q}^2\ \cos \mathbf{q}\cdot\mathbf{r}\ +\ B_f\ \mathbf{k}^2\ \cos \mathbf{k}\cdot\mathbf{r})\ C_1(z). \tag{A.4}$$

Note that $S_1(z) = \cos(z)$ with the boundaries at $z = \pm\ \pi/2$ due to our scaling conventions, that $C_1(z)$ is also close to a pure cosine, but with horizontal tangents at $z = \pm\ \pi/2$, and that $C_1'(z)$ is close to $S_2(z) = -\sin(2z)$. We neglect hereafter the contributions of the velocity po-

tential g to the horizontal velocity field. In effect g induces, in the two roll systems, an odd $v_\parallel$ component rather small as compared with the (odd) $v_\perp$ component kept in (A.3), since, from (B.3, B.4) of [1] and to lowest order:

$$\langle \frac{v_\parallel(\mathbf{q})}{v_\perp(\mathbf{q})} \rangle_z \ = -\frac{\tilde{g}(\mathbf{q})}{\tilde{f}(\mathbf{q})} \ \frac{1}{\pi} \int_{z=-\pi/2}^{z=\pi/2} \frac{S_2(z)}{C_1'(z)} \ dz \simeq -0.89 \frac{\tilde{g}(\mathbf{q})}{\tilde{f}(\mathbf{q})}.$$

For 5CB for instance, and all active wavevectors $\mathbf{q}$, we expect from (3.4) of [1] that $|\tilde{g}(\mathbf{q})/\tilde{f}(\mathbf{q})| < 0.22$, so that $|v_\parallel(\mathbf{q})/v_\perp(\mathbf{q})| \lesssim 0.20 \ll 1$.

From (A.2), we see that the warm and cold lines in rolls reduce to warm and cold points in the bimodal varicose, since $\theta(\mathbf{r}, 0)$ admits now maxima and minima at

$$\mathbf{r}_{warm} = n\mathbf{a} + m\mathbf{b} \quad , \ \mathbf{r}_{cold} = \Big(\frac{1}{2} + n\Big)\mathbf{a} + \Big(\frac{1}{2} + m\Big)\mathbf{b}$$

for all integers n, m. At these points, the horizontal velocity (A.3) cancels, and the vertical velocity presents also maxima and minima. These points corresponds to *sources* and *sinks*, and are shown by the black circles and squares in Figure 16. The left column of this figure shows, for $B/A = 0.45$, the level lines of $n_z(\mathbf{r})$, and the projection on the horizontal plane of some fluid trajectories obtained by numerical integration of $d\mathbf{r}/dt + \hat{\mathbf{z}}dz/dt = \mathbf{v}_h(\mathbf{r}, z) + \hat{\mathbf{z}}v_z(\mathbf{r}, z)$. These trajectories are always closed. The computations have been performed for 5CB and the typical wavevectors (4.3, 4.8); then $B_\theta/A_\theta = 1.2B/A, B_f/A_f = 1.7B/A$. These sources and sinks were observed in electroconvection (Fig. 3 of [15]). For visualization, it is interesting to plot also (right column of Fig. 16) the horizontal vorticity field in the mid-plane of the layer:

$$\boldsymbol{\Omega}_h(\mathbf{r}) = -A_\Omega \ \mathbf{b} \ \sin \mathbf{q} \cdot \mathbf{r} \ + \ B_\Omega \ \mathbf{a} \ \sin \mathbf{k} \cdot \mathbf{r} \qquad \text{(A.5)}$$

where $A_\Omega = |\mathbf{q}|/|\mathbf{b}|(\mathbf{q}^2 C_1(0) - C_1''(0))A_f, B_\Omega = |\mathbf{k}|/|\mathbf{a}|(\mathbf{k}^2 C_1(0) - C_1''(0))B_f$. Note that the prefactors $|\mathbf{q}|/|\mathbf{b}|$ and $|\mathbf{k}|/|\mathbf{a}|$ are equal (by definition of the reciprocal lattice), and that, for the typical wavevectors (4.3, 4.8), $B_\Omega/A_\Omega = 0.9B_f/A_f = 1.5B/A$. When B/A is increased, a progressive transition from the rolls of wavevector $\mathbf{q}$ (*i.e.* of axis parallel to $\mathbf{b}$) to the rolls of wavevector $\mathbf{k}$ (*i.e.* of axis parallel to $\mathbf{a}$) occurs. This transition happens in the following way for the horizontal vorticity: when $A \gg B$, $\boldsymbol{\Omega}_h$ is oriented along $\pm$ $\mathbf{b}$ for all $\mathbf{r}$; when B/A increases, $\boldsymbol{\Omega}_h$ rotates smoothly, from $\mathbf{b}$ to $-\mathbf{a}$ or $-\mathbf{b}$ to $\mathbf{a}$ in the core of the varicose cells, from $\mathbf{b}$ to $\mathbf{a}$ or $-\mathbf{b}$ to $-\mathbf{a}$ in the pinched regions; finally, when $B \gg A$, $\boldsymbol{\Omega}_h$ is now oriented along $\pm$ $\mathbf{a}$. This evolution was described in [15]; in fact Figure 3 there focuses on the specific symmetric case $\mathbf{k} = S(\mathbf{q})$. Note the existence of two lattices of points where $\boldsymbol{\Omega}_h$ cancels:

$$\mathbf{r}_+ = \Big(\frac{1}{2} + n\Big)\mathbf{a} + m\mathbf{b} \quad , \ \mathbf{r}_- = n\mathbf{a} + \Big(\frac{1}{2} + m\Big)\mathbf{b}$$

for all integers n, m. Around these singular points of the horizontal vorticity, the trajectories form "cross-like" structures which are reminiscent of *stagnation points* , as mentioned in [15]. In fact, at these points the horizontal velocity does cancel, but the vertical velocity only cancels in the case of a fully symmetric bimodal ($A = B$ and $\mathbf{k} = S(\mathbf{q})$).

References

1. E. Plaut, R. Ribotta, first part of this paper (weakly nonlinear models), Eur. Phys. J. B **5**, 265 (1998).
2. Q. Feng, W. Pesch, L. Kramer, Phys. Rev. A **45**, 7242 (1992).
3. E. Guyon, P. Pieranski, C.R. Acad. Sci. **274**, 656 (1972); E. Dubois-Violette, E. Guyon, P. Pieranski, Mol. Cryst. Liq. Cryst. **26**, 193 (1974).
4. See L.I. Berge, G. Ahlers, D.S. Cannell, Phys. Rev. E **48**, 3236 (1993), and also the contribution of G. Ahlers in A. Buka, L. Kramer, *Pattern formation in liquid crystals* (Springer-Verlag, New-York, 1996).
5. E. Plaut, R. Ribotta, Europhys. Lett. **38**, 441 (1997).
6. E. Plaut, A. Joets, R. Ribotta, J. Phys. III France **7**, 2459 (1997).
7. See *e.g.* P. Manneville, *Dissipative Structures and weak Turbulence* (Academic Press, New York, 1990).
8. MBBA turned out to be not a very stable material: we observed a decrease of 15% of the thresholds in MBBA over a period of 4 months; the reported value of α_{MBBA} is only compatible with the measurements of the first month.
9. D.A. Dunmur, W.H. Miller, J. Phys. France Colloq. **40**, C3-141 (1979).
10. W. Pesch, L. Kramer, Z. Phys. B - Cond. Mat. **63**, 121 (1986).
11. A. Joets, L. Kramer, R. Ribotta, J. Salan, W. Zimmerman, unpublished.
12. A. Tschammer, W. Pesch, private communication.
13. M. Kaiser, W. Pesch, Phys. Rev. E **48**, 4510 (1993).
14. L. Kramer, E. Bodenschatz, W. Pesch, W. Thom, W. Zimmermann, Liq. Cryst. **5**, 699 (1989).
15. R. Ribotta, A. Joets, J. Phys. France **47**, 739 (1986).
16. F.H. Busse, R.M. Clever, J. Fluid Mech. **91**, 319 (1979).
17. R. Yang, F.K. Browand, P. Coullet, P. Huerre, J. Fluid Mech. **248**, 403 (1993).
18. P.H. Bolomey, C. Dimitroupoulos, Mol. Cryst. Liq. Cryst **36**, 75 (1976).
19. A. Joets, R. Ribotta, J. Phys. France **47**, 595 (1986).
20. A. Belaidi, Ph. D. thesis, Université d'Orsay, 1998.
21. B. Janiaud, H. Kokubo, M. Sano, Phys. Rev. E **47**, R2237 (1993).
22. C. Mauguin, Bull. Soc. Fr. Min. **34**, 71 (1911).